[O III] line ratios and evolution of oxygen abundance with redshift using JWST-VLT-Keck observations

Vidit Bhandari,[1] Mingyi Xu,[2] Sultana N. Nahar,[2] Anil K. Pradhan [2,3]* and Kevin Hoy[4]

[1] *Department of Physics, Denison University, Granville, OH, USA.*

[2] *Department of Astronomy,* [3] *Chemical Physics Program, The Ohio State University, Columbus, OH, USA 43210.*

[4] *Chile.*

ABSTRACT

Understanding chemical evolution of galaxies has been dramatically revised by JWST observations up to high redshifts $z \sim 14$. Complemented by VLT and Keck observations, they reveal metal-rich systems forming within a few hundred million years after the Big Bang. Using new atomic data, we analyze or re-analyze reportedly observed O III line ratios in high-redshift galaxies to derive electron temperatures, densities, and oxygen abundance. In addition to [O III] temperature diagnostics, [O II] and [S II] ratios are employed for density constraints and contour plots of physical conditions. We examine the temperature–abundance relations and track the evolution of [12 + log(O/H)] with redshift. Our [O III] atomic model incorporates recombination-cascade contributions to forbidden lines using new level-specific recombination rate coefficients and transition probabilities, together with collision strengths computed in our earlier works. We find that individual galaxies show a large variation with electron temperature in the nebular range 5000-25000K and O-abundance down to 6.75 compared to the solar value 8.70. The oxygen abundances vs. z display a systematic decrease toward high-$z \sim 10$, with a best fit ranging from 8.25 to 7.50 from the present epoch at $z = 0$. The present analysis also considers possible (e + O IV) –> O III recombination-cascade contributions to [O III] forbidden lines, but is found to be negligible. That implicitly implies that the analysis refers to nebular H II regions per se, and not to possibly AGN contributions that might involve higher ionization states. We also explore AI Machine Learning models to predict and complement directly derived results, with preliminary simulations trained on observed flux ratios and PyNeb-simulated datasets that are promising but limited by current sample sizes. Future work may expand datasets and refine statistical models to establish robust constraints on early-universe chemical evolution.

Key words: keyword1 – keyword2 – keyword3

1 INTRODUCTION

Space-based observations of distant high-z galaxies by the James Webb Space Telescope (JWST) have definitively established that galaxy formation began much earlier than believed hitherto. That became evident from a number of clearly resolved atomic lines from several elements. Furthermore, since the observed spectra are in the near-IR range the observations can also be verified and complemented by ground-based observations, particularly by high-resolution spectrographs at large telescopes such as Keck and Very Large Telescope (VLT) observatories. Thus optical or even near-UV lines are observable from red-shifted objects. Since JWST spectra became available, it was noticed that several well-known lines of oxygen ions were prominent in the spectra of galaxies out to z~ 10 or greater. As oxygen is one of the most common elements, its abundance would therefore be a reliable indicator of the chemical evolution of the universe if determined accurately and from a sufficient number of galaxies. In our sample we consider the earliest one at $z \sim 10$ (Abdurro'uf et al. 2024, Hsiao et al. 2025, Hsiao et al. 2024), and the latest at $z \sim 1$ (Welch et al. 2024).

One oxygen ion, O III, well-known in observations from nebular and AGN H II regions, stands out in many of these JWST observations. The forbidden [O III] lines have been studied extensively and are used widely as temperature diagnostics in H II regions in the range 1000-20,000 K (??????). In addition, forbidden [O II] and [S II] lines are employed as electron density diagnostic. Together, these ions provide temperature-density information which, in turn, can be parametrized to derive oxygen abundance since only a few ionization states are involved. Useful expressions dependent on temperature and density have long been utilized obtain abundances in H II regions (e.g. Izotov *et al.* 2006, Mendez-Delgado *et al.* 2023).

A recent work has applied strong line calibration on deriving 12 + log(O/H) versus z relation out to z~ 3.3 using data from earlier instruments such as Keck for certain masses of galaxies (Jain et al. 2025). The JWST data with considering the theoretical atomic models is more accurate to consider high redshift galaxies out to z ~ 10.

The primary requirement in order to employ theoretical models to analyze observations is accurate atomic data for relevant physical processes. In the case of forbidden lines, which usually arise from transitions among low-lying energy levels, those data entail electron impact excitation and radiative transition probabilities. The dominant

transitions are among levels of the ground configuration of the same parity via magnetic dipole (M1) and electric quadruple (E2) transitions. The high-precision atomic data have been computed for all ions under study: O II , O III and S II (??????????). We employ these data in a spectral modeling code SPECTRA that constructs a radiative-collisional atomic model with a 5-level energy structure to obtain line emissivities and ratios. A new extension of SPECTRA is to extend the atomic model to include level-specific (e + ion) recombination coefficients from accurate R-matrix calculations (Hoy *et al.* 2023, Nahar ???????). The extended collisional-radiative-recombination (CRR) model incorporates (e + ion) recombination to a number of excited levels, and radiative decays therefrom, into the upper levels that give rise to the observed forbidden lines.

2 OBSERVATIONAL DATA ANALYSIS

Spectral data for 30 galaxies observed with JWST/NIRSpec, ground-based observations of 5 galaxies from Keck/KCWI/NIRSPEC/MOSFIRE, 7 galaxies from VLT/Shooter, 1 galaxy from CLASSY, and 1 galaxy from MOSDEF was analyzed (see References). In addition, data from a few other ground-based instruments was also obtained from literature. Detailed information on data sources is given in Appendices Table A1 and Table A2, along with reported quantitative fluxes for [O III], [O II] and [S II] lines, as well as H β fluxes.

The JWST line data in our collection are all from $z > 1$. For analyzing some galaxies for approximate comparison in the low-z region, we added a few galaxies from ground-based observations. The data used for lower redshift ground-based observations does not include all ground-based observations until the present eopch but a representative sample of a few points. For the galaxies that appears twice in the tables, they are analyzed using different sets of line fluxes data, as shown in Table A1. The results are arranged in the same order when reproduced in Table A3.

We collected the data for galaxies whose observed fluxes have been reported for determining spectral properties, namely unblended [O II] 3729,3726 or unblended [S II] 6717,6732 fine structure doublet formed by atomic structure and transitions $^4S^o - ^2D^o_{3/3,5/3}$ that are standard density diagnostics. The temperature diagnostic [O III] 4363,5007 lines due to the atomic transitions $^1D_2 - ^1S_0$ and $^3P^o_2 - ^1D_2$ respectively, that have been identified and extracted until recently available observations.

There are several cases where there are some lines missing from papers in literature. However, our line ratios analysis attempts to estimate their intensities from theoretical line emissivity calculations described below. In particular, if [O III] 4959 is missing (necessary for the Oxygen abundance formula from Izotov et al. (2006)), we calculate its intensity since the ratio [O III] 5007/4959 = 2.88 is constant. That is because both transitions originate from the same upper level and the intensity ratio is determined by their respective A-values **?**, and independent of environment temperature or density. In cases where [O II] 3729,3726 lines are missing then we employ the [O II]7320,7332 lines due to forbidden transitions $2s^2p^3(^2D^o_{3/2} - ^2P^o_{1/2,3/2}$ (c.f. Izotov *et al.* 2006).

3 THEORY & COMPUTATIONAL METHOD

The calculations described in this paper employ high-accuracy atomic data computed using the powerful R-matrix method and subsidiary codes described in this section.

3.1 Energy Levels & Einstein A Coefficients

The energy level data for OIII is computed using the R-matrix method (Nahar 1998) but substituted using observed energies where available from the National Institute of Standards and Technology (NIST) Atomic Spectra Database (www.nist.gov). The transition probabilities and A-coefficients are also obtained from previous R-matrix calculations and archived in the database Nahar-OSU-Radiative-Atomic-Database (NORAD; http://norad.astronomy.osu.edu).

Fig. 1 shows the atomic model of OIII including the 10 well-know forbidden transitions among the 5 even-parity levels of the ground configuration $1s^2 2s^2 2p^2 : \, ^3P_{0,1,2}, ^1D_2, ^1S_0$. These levels are considered for collisional excitation. In addition, and for including (e + ion) recombiation into higher levels and radiative cascades therefrom, excited electronic configurations up to n = 10 are included.

3.2 Electron Impact Excitation

We consider collision strengths and Maxwellian averaged rate co-efficients for the forbidden [O III] ground configuration transitions as in earlier works (Palay *et al.* 2012, Storey and Sochi 2015). The two sets of data agree within a few per cent throughout most of the temperature range of interest in nebulae, but differ somewhat at low electron temperatures $T_e < 1000K$ where the latter are to be preferred. That is because Storey and Sochi (2015) include additional correlation in the wavefunction expansion for the [O III] levels that include the excited configuration $1s^2 2p^6$ that correlates with the quasi-degenerate $^1S_0$ level of the ground configuration $1s^2 2s^2 2p^r$. That additional correlation gives rise to somewhat lower resonance structures near the excitation thresholds up to the $^1S_0$ level, resulting Maxwellian averaged colllision strengths that differ from Palay *et al.* (2012). However, as we show later, the line emissivity ratios in the range of interest herein is hardly affected in using the two sets.
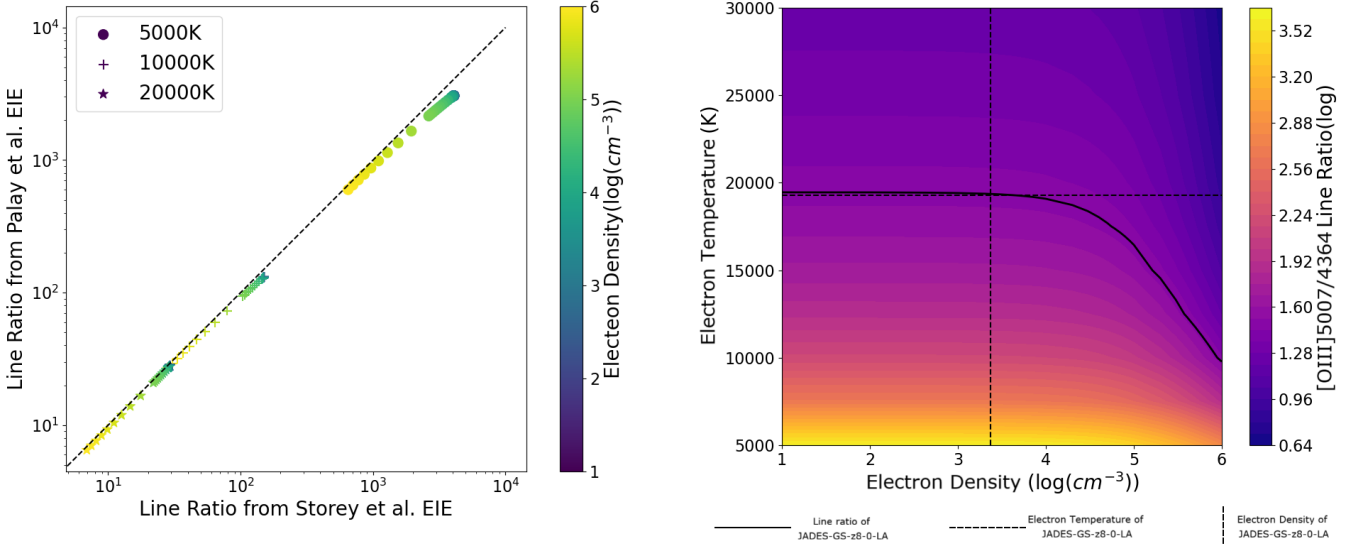
3.3 Electron-ion recombination

In order to discern possible effects due to (e + ion) recombination, i.e. $(e + O\,iv) \rightarrow O\,iii$, we considerably expand the set of excited energy levels of O III . That enables recombination into excited levels followed by radiative cascades to the 5 levels that give rise to the observed forbidden lines via dipole allowed transitions down to upper levels (Sultana: please fill in this subsection).
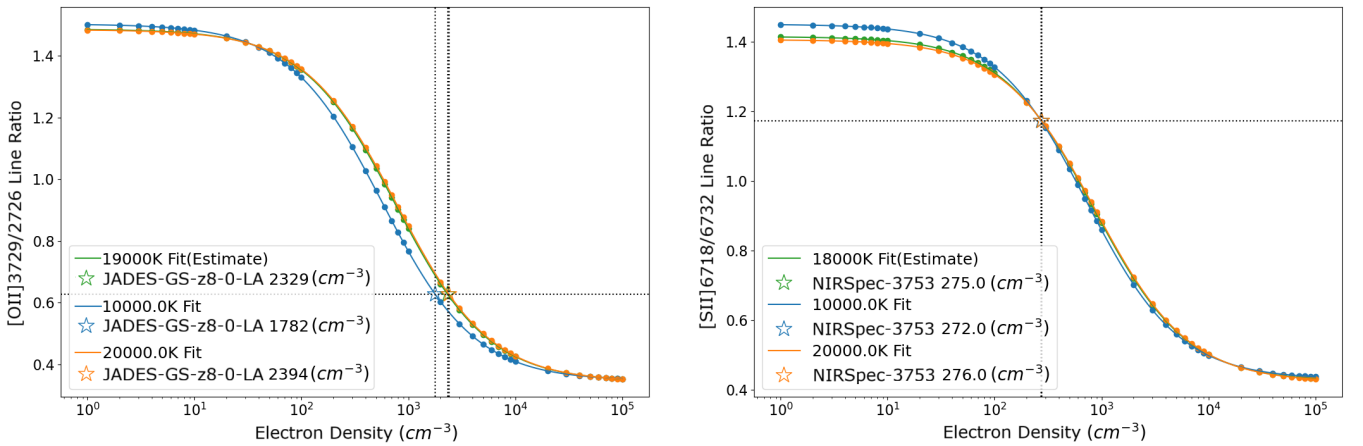
3.4 Line Emissivities & Ratios

The CRR model is incorporated in a code SPECTRA that computes line emissivities and diagnostic ratios from the data described above. There are two versions of SPECTRA in Fortran and C++ that have been compared against each other (Hoy *et al.* 2023).

The procedure adopted relies on the canonical [O III] 5007/4363 line ratio that is known to be dependent on electron temperature, and the [O II] 3729/3726 and [S II] 6717/6731 line ratios that are sensitive to electron density. However, as we note below, there are two sets of [O III] theoretical collision strengths available in literature: Palay *et al.* (2012) and Storey and Sochi (2015). We compute and compare the two sets in Fig. 1a, and find little difference in the nebular temperature range under consideration (see section Electron Impact Excitation below). Using the later Storey and Sochi (2015) data, and [O II] collision strengths (????) and [S II] collision strengths (????), we construct a contour plot of the full electron temperature-density range shown in Fig. 1b. The atomic data employed in the present work is as follows.

Figure 1. (Left)Comparison between the $OIII5007/4363$ line ratio results of SPECTRA code by inputting Storey & Sochi (2015) and Palay et al. (2012) effective collisional strength data. (Right)$[OIII]5007/4363$ line ratio contours results of SPECTRA code by inputting Storey & Sochi (2015) effective collisional strength data.

Figure 2. (Left)$[OII]3729/3726$ Density Diagnotics. (Right)$[SII]6718/6732$ Density Diagnotics.

4 RESULTS

For oxygen abundance calculation, we adopt two different empirical formulae by Izotov et al. (2006) and Méndez-Delgado et al. (2023) respectively.

4.1 Formula by Izotov et al. (2006)

The inputs for this formula are relative line fluxes to Hβ, N_e, and T_e. Firstly, it defines $t = 10^{-4}T_e([OIII])$ and $x = 10^{-4}N_e t^{-0.5}$. The following are the formula:

$$12 + \log(O^+/H^+) = \log(\frac{OII3727}{H\beta}) + 5.961$$
$$+ \frac{1.676}{t} - 0.40\log(t) - 0.034t + log(1 + 1.35x) \quad (1)$$

$$12 + \log(O^+/H^+) = \log(\frac{OII7320 + OII7330}{H\beta}) + 6.901$$
$$+ \frac{2.487}{t} - 0.483\log(t) - 0.013t + log(1 - 3.48x) \quad (2)$$

$$12 + \log(O^{2+}/H^+) = \log(\frac{OIII4959 + OIII5007}{H\beta}) + 6.200$$
$$+ \frac{1.251}{t} - 0.55\log(t) - 0.014t \quad (3)$$

OII3727 represents the total(blended) relative flux of OII3726 and OII3729 to Hβ. If OII 3727 is available, we could use (1) to calculate the OII abundance. If OII 3727 is not available, we could use OII7320 and OII7330 relative fluxes by (2) to calculate the OII abundance.

Also, using (3) with OIII4959 relative flux, OIII5007 relative flux, and electron temperature, we can calculate OIII abundance.

Once we have the abundance for singly ionized state(OII) and

doubly ionized state(OIII), we can add them up as (4) to get the total oxygen abundance.

$$\frac{O}{H} = \frac{O^+}{H^+} + \frac{O^{2+}}{H^+} \tag{4}$$

For a specific galaxy PJ308-21, its original paper Decarli et al. (2024) gives neither [O II] λ 3729+λ 3726 nor [O II] λ 7320+λ 7330 fluxes for using Izotov et al. (2006) oxygen abundance formula (1) or (2) to calculate $12 + \log(O^+/H^+)$. We then assume three different values for [O II] λ 3729+λ 3726 relative flux to Hβ: 0.5, 1.0, and 2.0. This assumption is based on the fact that most of other galaxies we examined have [O II] λ 3729+λ 3726 relative flux to Hβ around the range 0.5 to 2.0. Only the abundance formulae (1) from Izotov et al. (2006) are used with this assumed [O II] λ 3729+λ 3726 relative flux for PJ308-21, and density determination was done by using [S II] lines. We find that results under such assumption are quite similar, $12 + \log(O/H) = 7.99, 8.02$ and 8.07 respectively. The another result for PJ308-21, by using another oxygen abundance formula from Méndez-Delgado et al. (2023)(will be discussed in 4.3), is $12 + \log(O/H) = 7.95$, which is quite similar to the results by assuming [O II] λ 3729+λ 3726 flux relative to Hβ with using Izotov et al. (2006) oxygen abundance formula (1). The first result $12 + \log(O/H) = 7.99$ is then adopted in the abundance over temperature, redshift, and lookback time plots.

4.2 Formula by Méndez-Delgado et al. (2023)

$$12 + \log(O/H) = (-1.07 \pm 0.09) \times 10^{-4} T_0(H^+) + (9.44 \pm 0.08) \tag{5}$$

4.3 AI Model

Our machine learning analysis reveals varying degrees of success in predicting stellar properties from spectroscopic features. For electron temperature (Te) predictions, the model achieves an R^2 of 0.279, indicating moderate predictive capability with systematic scatter around the 1:1 relationship. The residual analysis shows relatively uniform distribution around zero, suggesting no strong systematic bias, though the prediction errors range from approximately -4000 to +2000 K. Feature importance analysis identifies the O III ratio as the dominant predictor, contributing over 50

In contrast, the logOH predictions demonstrate poor performance with a negative R^2 of -0.567, indicating the model performs worse than a simple mean predictor. The residual plot reveals systematic deviations from the expected relationship, with residuals showing a pronounced asymmetric distribution heavily weighted toward positive values (residuals 0.15). This suggests fundamental limitations in the current feature set or model architecture for metallicity predictions. The feature importance hierarchy mirrors that of the Te model, with O III ratio dominating, but the overall predictive framework proves inadequate for this target variable.

Our dataset encompasses 37 galaxies with complete Te measurements and varying data completeness across different spectroscopic features. The sample spans redshifts from z2 to z8, with electron temperatures ranging from 12,000 to 20,000 K and metallicities from 12+log(O/H) 2 to 8. Correlation analysis reveals expected relationships: a moderate positive correlation between Te and redshift (r=0.18), weak negative correlations between metalicity and both Te (r=-0.083) and redshift (r=0.21), and strong positive correlation between O III and Si II ratios (r=0.24). The data quality assessment shows most galaxies achieve high completeness scores (>0.8), though

several systems show intermediate completeness (0.4-0.6), reflecting the observational challenges inherent in high-redshift spectroscopy

5 DISCUSSION

Lookback time was calculated from redshifts by Astropy Planck18 instance of FlatΛCDM cosmology.
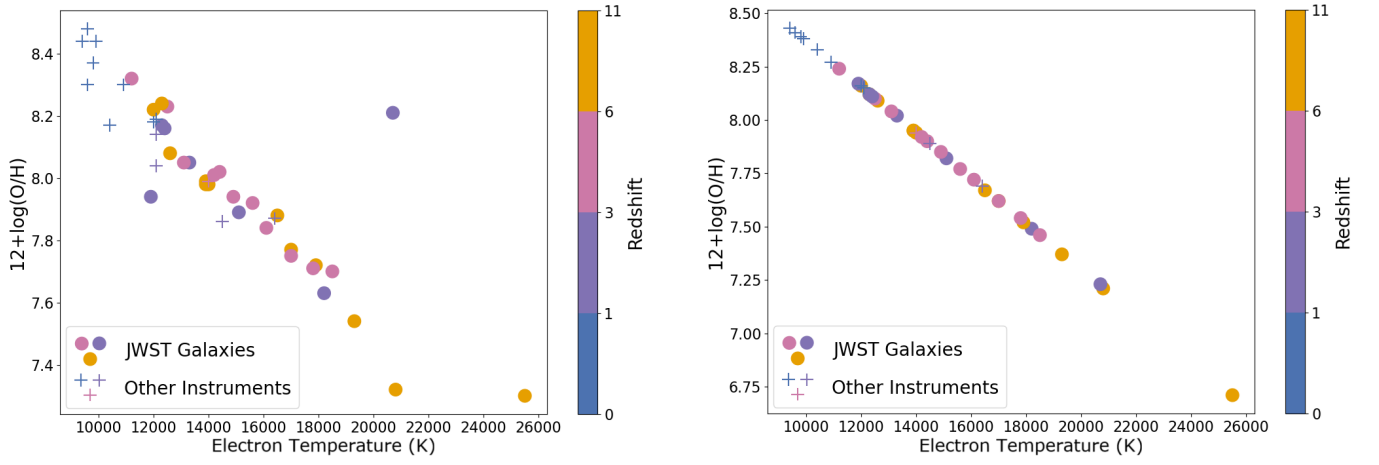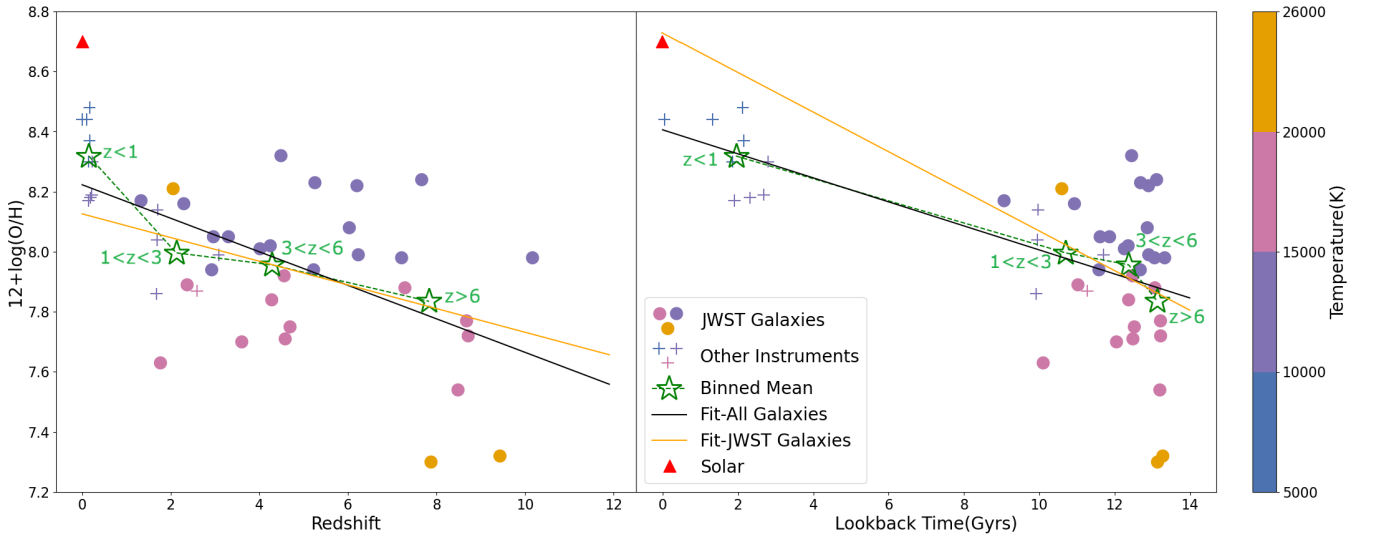
6 CONCLUSIONS

DATA AVAILABILITY

REFERENCES

Abdurro'uf et al., 2024, JWST NIRSpec High-resolution Spectroscopy of MACS0647-JD at z=10.167: Resolved [OII] Doublet and Electron Density in an Early Galaxy (arXiv:2404.16201), https://arxiv.org/abs/2404.16201

Acharyya A., et al., 2019, Monthly Notices of the Royal Astronomical Society, 488, 5862–5886

Arellano-Córdova K. Z., et al., 2025, The JWST EXCELS survey: direct estimates of C, N, and O abundances in two relatively metal-rich galaxies at $z \simeq 5$ (arXiv:2412.10557), https://arxiv.org/abs/2412.10557

Astropy Collaboration et al., 2013, A&A, 558, A33

Astropy Collaboration et al., 2018, AJ, 156, 123

Astropy Collaboration et al., 2022, ApJ, 935, 167

Berg D. A., et al., 2022, ApJS, 261, 31

Bhattacharya S., Arnaboldi M., Gerhard O., Kobayashi C., Saha K., 2025, Unveiling galaxy chemical enrichment mechanisms out to z 8 from direct determination of O Ar abundances from JWST/NIRSPEC spectroscopy (arXiv:2408.13396), https://arxiv.org/abs/2408.13396

Bunker A. J., et al., 2024, Astronomy & Astrophysics, 690, A288

Chen Y., et al., 2024, Robust Nitrogen and Oxygen Abundances of Haro 3 from Optical and Infrared Emission (arXiv:2405.18476), https://arxiv.org/abs/2405.18476

Clarke L., et al., 2023, Ultra-deep Keck/MOSFIRE spectroscopic observations of $z \sim 2$ galaxies: direct oxygen abundances and nebular excitation properties (arXiv:2305.07781), https://arxiv.org/abs/2305.07781

Curti M., et al., 2022, Monthly Notices of the Royal Astronomical Society, 518, 425–438

Curti M., et al., 2025, Astronomy & Astrophysics, 697, A89

Decarli R., et al., 2024, Astronomy & Astrophysics, 689, A219

Gburek T., et al., 2019, The Astrophysical Journal, 887, 168

Harikane Y., et al., 2025, JWST ALMA Joint Analysis with [OII]$\lambda\lambda$3726,3729, [OIII]λ4363, [OIII]88μm, and [OIII]52μm: Multi-Zone Evolution of Electron Densities at $z \sim 0 - 14$ and Its Impact on Metallicity Measurements (arXiv:2505.09186), https://arxiv.org/abs/2505.09186

Harris C. R., et al., 2020, Nature, 585, 357

Hsiao T. Y.-Y., et al., 2024, JWST MIRI detections of Hα and [O III] and direct metallicity measurement of the $z = 10.17$ lensed galaxy MACS0647$-$JD (arXiv:2404.16200)

Hsiao T. Y.-Y., et al., 2025, First direct carbon abundance measured at $z > 10$ in the lensed galaxy MACS0647$-$JD (arXiv:2409.04625), https://arxiv.org/abs/2409.04625

Hunter J. D., 2007, Computing in Science & Engineering, 9, 90

Figure 3. Oxygen Abundance Evolution with temperature using Izotov et al. (2006) formula (Left) and Méndez-Delgado et al. (2023) formula (Right)

Figure 4. Oxygen Abundance Evolution with redshift and lookback time using Izotov et al. (2006) formula

Inkenhaag A., et al., 2025, First joint absorption and T_e-based metallicity measured in a GRB host galaxy at $z = 4.28$ using JWST/NIRSpec (arXiv:2506.08114), https://arxiv.org/abs/2506.08114

Isobe Y., Ouchi M., Nakajima K., Harikane Y., Ono Y., Xu Y., Zhang Y., Umeda H., 2023, Redshift Evolution of the Electron Density in the ISM at $z \sim 0 - 9$ Uncovered with JWST/NIRSpec Spectra and Line-Spread Function Determinations (arXiv:2301.06811), https://arxiv.org/abs/2301.06811

Izotov Y. I., Stasińska G., Meynet G., Guseva N. G., Thuan T. X., 2006, Astronomy & Astrophysics, 448, 955–970

Jain S., et al., 2025, A Uniform Analysis of Gas-phase Metallicity Evolution with 1-3 Gyr Time Sampling over the Past 12 Billion Years (arXiv:2508.18369), https://arxiv.org/abs/2508.18369

Li S., et al., 2025, The Astrophysical Journal Letters, 979, L13

Loaiza-Agudelo M., Overzier R. A., Heckman T. M., 2020, The Astrophysical Journal, 891, 19

Matsuoka Y., et al., 2025, SHELLQs. Bridging the gap: JWST unveils obscured quasars in the most luminous galaxies at z > 6 (arXiv:2505.04825), https://arxiv.org/abs/2505.04825

Mingozzi M., et al., 2022, The Astrophysical Journal, 939, 110

Morishita T., et al., 2025, Metallicity Scatter Originating from Sub-

kiloparsec Starbursting Clumps in the Core of a Protocluster at z=7.88 (arXiv:2501.11879), https://arxiv.org/abs/2501.11879

Méndez-Delgado J. E., Esteban C., García-Rojas J., Kreckel K., Peimbert M., 2023, Nature, 618, 249–251

Nakajima K., Ouchi M., Isobe Y., Harikane Y., Zhang Y., Ono Y., Umeda H., Oguri M., 2023, JWST Census for the Mass-Metallicity Star-Formation Relations at z=4-10 with the Self-Consistent Flux Calibration and the Proper Metallicity Calibrators (arXiv:2301.12825), https://arxiv.org/abs/2301.12825

Palay E., Nahar S. N., Pradhan A. K., Eissner W., 2012, Monthly Notices of the Royal Astronomical Society: Letters, 423, L35–L39

Rogers N. S. J., Strom A. L., Rudie G. C., Trainor R. F., Raptis M., von Raesfeld C., 2024, CECILIA: Direct O, N, S, and Ar Abundances in Q2343-D40, a Galaxy at $z \sim 3$ (arXiv:2312.08427), https://arxiv.org/abs/2312.08427

Sanders R. L., et al., 2016, The Astrophysical Journal Letters, 825, L23

Sanders R. L., Shapley A. E., Topping M. W., Reddy N. A., Brammer G. B., 2023, Direct Te-based Metallicities of z=2-9 Galaxies with JWST/NIRSpec: Empirical Metallicity Calibrations Applicable from Reionization to Cosmic Noon (arXiv:2303.08149), https://arxiv.org/abs/2303.08149

Figure 5. Oxygen Abundance Evolution with redshift and lookback time using Méndez-Delgado et al. (2023) formula

Stiavelli M., et al., 2024, What can we learn from the Nitrogen abundance of High-z galaxies? (arXiv:2412.06517), https://arxiv.org/abs/2412.06517

Storey P. J., Sochi T., 2015, Monthly Notices of the Royal Astronomical Society, 449, 2974–2979

Virtanen P., et al., 2020, Nature Methods, 17, 261

Welch B., et al., 2024, TEMPLATES: Direct Abundance Constraints for Two Lensed Lyman-Break Galaxies (arXiv:2401.13046), https://arxiv.org/abs/2401.13046

Welch B., et al., 2025, The Sunburst Arc with JWST: III. An Abundance of Direct Chemical Abundances (arXiv:2405.06631), https://arxiv.org/abs/2405.06631

Witstok J., et al., 2024, Monthly Notices of the Royal Astronomical Society, 536, 27–50

Zhang Y., Morishita T., Stiavelli M., 2025, Potential Nitrogen Enrichment via Direct-Collapse Wolf-Rayet Stars in a $z = 4.7$ Star-Forming Galaxy (arXiv:2502.04817), https://arxiv.org/abs/2502.04817

Zhu C., et al., 2025, The Physical Origin of Extreme Emission Line Galaxies at High redshifts: Strong [OIII] Emission Lines Produced by Obscured AGNs (arXiv:2410.12198), https://arxiv.org/abs/2410.12198

APPENDIX A: DATA COLLECTION OF ANALYSIS RESULTS AND LINE FLUXES FROM LITERATURE

Table A1. A holistic table of line fluxes from other papers. All line fluxes are normalized by Hβ = 1.

Galaxy	z	OII3726	OII3729	OIII4363	OIII4959	OIII5007	SII6718	SII6732	OII7320	OII7330	Hβ Flux $(erg\ s^{-1}\ cm^{-2})$
Haro3	0.003208	1.243	1.577	0.02521	1.361	4.016	0.1461	0.1172	-	-	-
J0021+0052	0.09839	0.6407	0.7217	0.02202	1.537[c]	4.427	0.1819	0.1312	0.02554	0.01982	$2.271 \cdot 10^{-14}$
J032845.99+011150.8	0.142181	2.154[a]	-	0.01280	0.7333	2.294	0.2849	0.2191	0.02312	0.01920	$2.812 \cdot 10^{-15}$
J015028.39+130858.4	0.146712	2.220[a]	-	0.01650	0.7424	2.221	0.2570	0.2205	0.01881	0.01568	$6.059 \cdot 10^{-15}$
J124509.05+104340.1	0.165569	1.775[a]	-	0.02845	1.718	5.122	0.1714	0.1435	0.02856	0.02243	$8.648 \cdot 10^{-15}$
J005527.45−002148.7	0.167449	2.008[a]	-	0.02228	1.236	3.673	0.1768	0.1573	0.03513	0.02718	$1.611 \cdot 10^{-14}$
J101629.88+073404.9	0.18271	2.271[a]	-	0.05832	1.729	5.236	0.1475	0.1231	0.02264	0.01852	$7.288 \cdot 10^{-15}$
J082247.66+224144.0	0.216226	2.090[a]	-	0.06771	1.924	5.814	0.1329	0.1225	0.03747	0.02757	$8.994 \cdot 10^{-15}$
J084034.10+134451.3	0.226961	1.785[a]	-	0.04537	1.784	5.353	0.1842	0.1465	0.02768	0.02191	$2.601 \cdot 10^{-15}$
GOODS-N-14595	1.67596	0.5759	0.6161	0.08929	1.692	4.960	0.2500	<0.5446	-	-	$2.240 \cdot 10^{-17}$
GOODS-N-8240	1.6909	0.5944	0.6285	0.04954	1.458	4.434	<0.9659	<5.399	-	-	$3.230 \cdot 10^{-17}$
RCSGA032727-132609	1.7	1.133	0.9876	0.05637	1.543	4.900	0.1448	0.1066	-	-	$4.495 \cdot 10^{-15}$
SGAS1723+34	1.3293	-	-	0.07480	2.084	6.239	0.1447	0.1076	0.02103	0.01935	$1.845 \cdot 10^{-15}$
NIRSpec3753	1.768	2.692[a]	-	0.1169	1.270	4.040	0.2770	0.2361	-	-	$8.810 \cdot 10^{-18}$
CEERS-3506	2.055	-	-	0.2350	2.530	6.510	0.01360	0.02230	0.007100	0.004200	$2.210 \cdot 10^{-17}$
CEERS-3788	2.295	0.4170	0.4590	0.08800	2.370	7.010	0.3720	0.2330	-	-	$6.600 \cdot 10^{-19}$
Sunburst Arc	2.37	0.2900	0.2200	0.1380	2.200	6.800	0.03900	0.04300	0.03000	0.02200	$1.920 \cdot 10^{-16}$
A1689-217	2.5918	1.156	1.339	0.1094	2.156	6.210[c]	-	-	-	-	$1.721 \cdot 10^{-16}$
SGAS1226+21	2.925	-	-	<0.04707	1.320	4.327	0.3045	0.2917	<0.006973	<0.006973	$8.650 \cdot 10^{-18}$
Q2343-D40	2.963	-	-	0.08700	1.993	5.914	0.1310	0.09700	0.02500	0.02000	-
Q2343-D40	2.963	-	-	0.04000	2.254	7.075	0.1310	0.09700	0.02500	0.02000	-
COSMOS-1908	3.08	0.2309	0.2309	0.1186	2.288	7.055	-	-	-	-	$4.720 \cdot 10^{-17}$
CEERS-11088	3.302	1.681[a]	-	0.05737	2.041	6.052	0.2147	0.1714	0.07257[b]	-	$2.632 \cdot 10^{-17}$
CEERS-11088	3.302	0.5200	0.4700	0.08800	1.936	6.233	0.5830	0.2570	-	-	-
JADES-19519	3.604	0.3790	0.5330	0.2010	2.279	6.782	-	-	-	-	-
GTO1199-150880	4.247	0.2140	0.2610	0.1540	2.559	7.725	-	-	-	-	-
GRB050505	4.28	1.006[a]	-	0.1358	10.26[d]	-	0.08447	0.06849	-	-	$8.760 \cdot 10^{-18}$
CEERS-1665	4.482	0.7037	0.9722	0.1389	2.065	6.046	0.2778	0.2037	<0.08772[b]	-	$1.080 \cdot 10^{-17}$
CEERS-1665	4.488	1.514[a]	-	0.06532	2.214	6.827	0.1512	0.1243	-	-	$2.679 \cdot 10^{-17}$
CEERS-1746	4.56	0.5120	0.3520	0.06700	2.338	7.336	0.3100	0.2030	<0.1425[b]	-	-
GLASS-150029	4.584	1.120[a]	-	0.1624	2.251	7.604	0.09117	0.09687	-	-	$3.510 \cdot 10^{-18}$
GLASS-150029	4.584	0.1780	0.2070	0.1840	2.328	6.588	-	-	-	-	-
ID60001	4.6928	0.1827	0.2373	0.1530	2.221	6.316	-	-	-	-	-
EXCELS-121806	5.225	0.5650[a]	-	0.1640	2.170	6.470	0.04374	0.03645	-	-	$8.230 \cdot 10^{-18}$
EXCELS-70864	5.255	0.8411[a]	-	0.1339	2.327	6.826	0.05920	0.04835	-	-	$4.054 \cdot 10^{-18}$
J1211-0118	6.031	0.9760	1.163	<0.06200	1.605	4.783	-	-	-	-	$1.260 \cdot 10^{-17}$
J0217-0208	6.204	0.8930	0.6030	0.07500	2.004	6.567	-	-	-	-	$1.880 \cdot 10^{-17}$
J0217-0208	6.204	0.8930	0.6030	0.09592	2.234[c]	6.433	0.08931	0.09482	-	-	$9.070 \cdot 10^{-18}$
PJ308-21	6.2342	0.5/1.0/2.0[ac]	-	0.1139	2.293	6.873	0.1418	0.1721	-	-	$1.650 \cdot 10^{-17}$
SXDF-NB1006-2	7.212	0.2660	0.2390	0.1130	2.262	6.741	-	-	-	-	$8.550 \cdot 10^{-18}$
GLASS-10021	7.286	0.3378	0.4730	0.1980	2.696	8.284	-	-	-	-	$7.400 \cdot 10^{-18}$
ERO6355	7.6651	0.5104	0.3896	0.1000	2.660	8.290	-	-	-	-	$2.110 \cdot 10^{-18}$
ZD12	7.8762	0.3300	0.2791	0.2529	7.051[d]	-	-	-	-	-	$6.090 \cdot 10^{-19}$
JADES-GS-z8-0-LA	8.48523	0.1402	0.08785	0.1776	1.836	5.470	-	-	-	-	$3.210 \cdot 10^{-19}$
CEERS-1019	8.6791	0.2084	0.1781	0.1780	2.262	7.011	-	-	-	-	$1.017 \cdot 10^{-17}$
JADES-GS-z8-1-LA	8.71523	0.2667	0.2309	0.2010	2.401	7.153	-	-	-	-	$8.360 \cdot 10^{-19}$
JADES-GS-z9-0	9.4327	0.07825	0.07294	0.1790	1.756	4.955	-	-	-	-	$7.540 \cdot 10^{-19}$
MACS0647-JD1	10.167	0.1038	0.07022	0.1130	2.396[c]	6.900	-	-	-	-	$3.275 \cdot 10^{-18}$

[a] This is the blended flux for OII3726+OII3729.
[b] This is the blended flux for OII7320+OII7330.
[c] This is not come from papers, it is come from assumptions as shown in the text of Appendix A
[d] This is the blended flux for OIII4959+OIII5007.

Table A2. Line flux data sources of galaxies

Source	Instrument	Adopted line flux data of galaxies
Acharyya et al. (2019)	Keck/NIRSPEC	All data of RCSGA032727-132609.
Chen et al. (2024)	Keck/KCWI	All data of Haro3.
Clarke et al. (2023)	Keck/MOSFIRE	All data of GOODS-N-14595 and GOODS-N-8240.
Loaiza-Agudelo et al. (2020)	VLT/XShooter	All data of J032845.99+011150.8, J015028.39+130858.4, J124509.05+104340.1, J005527.45–002148.7, J101629.88+073404.9, J082247.66+224144.0,and J084034.10+134451.3.
Mingozzi et al. (2022)	CLASSY	All data of J0021+0052.
Sanders et al. (2016)	MOSDEF	All data of COSMOS-1908.
Arellano-Córdova et al. (2025)	JWST/NIRSpec	All data of EXCELS-121806 and EXCELS-70864.
Bhattacharya et al. (2025)	JWST/NIRSpec	All data of CEERS-3788, the second row of CEERS-11088, the first row of GLASS-150029, JADES-19519, and the second row of CEERS-1665. OIII4363, OIII4960, and OIII5008 line fluxes of the second row of Q2343-D40.
Decarli et al. (2024)	JWST/NIRSpec	All data of PJ308-21.
Harikane et al. (2025)	JWST/NIRSpec	All data of J1211-0118, SXDF-NB1006-2, and first row of J0217-0208. Line fluxes of OII 3726 and 3729 lines of the second row of J0217-0208
Sanders et al. (2023)	JWST/NIRSpec	Blended line flux of OII 3726 and 3729 lines and all other line flux data of CEERS-1019. All data of CEERS-1746, the first row of CEERS-11088, and the first row of CEERS-1665.
Isobe et al. (2023)	JWST/NIRSpec	OII 3726 and 3729 lines ratio of CEER-1019, ERO6355, GLASS-160133, and the second row of GLASS-150029.
Curti et al. (2022)	JWST/NIRSpec	Blended flux of OII 3726 and 3729 lines and all other line flux data of ERO6355.
Hsiao et al. (2025)	JWST/NIRSpec	Line flux OIII 5007(=226 · 10^{-19} erg s^{-1} cm^{-2}) of MACS0647-JD1.
Hsiao et al. (2024)	JWST/NIRSpec	OIII5007/Hbeta(=6.9) ratio of MACS0647-JD1.
Abdurro'uf et al. (2024)	JWST/NIRSpec	OII3726, OII3729, and OIII4363 line fluxes of MACS0647-JD1.
Welch et al. (2024)	JWST/NIRSpec	All data of SGAS1226+21 and SGAS1723+34.
Welch et al. (2025)	JWST/NIRSpec	All data of Sunburst Arc.
Matsuoka et al. (2025)	JWST/NIRSpec	All data except for fluxes of OII 3726 and 3729 lines of the second row of J0217-0208.
Rogers et al. (2024)	JWST/NIRSpec	All data of the first row of Q2343-D40. SII6718, SII6732, OII7320, and OII7330 line fluxes of the second row of Q2343-D40.
Nakajima et al. (2023)	JWST/NIRSpec	Blended line flux of OII 3726 and 3729 lines and all other line flux data of the second row of GLASS-150029, GLASS-10021, and GLASS-160133.
Curti et al. (2025)	JWST/NIRSpec	All data of JADES-GS-z9-0.
Witstok et al. (2024)	JWST/NIRSpec	All data of JADES-GS-z8-1-LA and JADES-GS-z8-0-LA.
Zhu et al. (2025)	JWST/NIRSpec	All data of CEERS-3506
Gburek et al. (2019)	Keck/MOSFIRE	All data of A1689-217.
Bunker et al. (2024)	JWST/NIRSpec	All data of NIRSpec3753.
Inkenhaag et al. (2025)	JWST/NIRSpec	All data of GRB050505.
Li et al. (2025)	JWST/NIRSpec	OII 3726 and 3729 lines ratio of GLASS-10021.
Morishita et al. (2025)	JWST/NIRSpec	All data of ZD12.
Stiavelli et al. (2024)	JWST/NIRSpec	All data of GTO1199-150880.
Zhang et al. (2025)	JWST/NIRSpec	All data of ID60001.

Table A3. A holistic table of analysis results by using Storey & Sochi (2015) EIE data

Galaxy	Instrument	z	12 + log(O/H) Izotov Formula	12 + log(O/H) MD Formula[d]	12 + log(O/H) Original Papar	$T_e[OIII]$ (K)	$N_e[OII]$ (cm^{-3})	$N_e[SII]$ (cm^{-3})
Haro3	Keck/KCWI	0.003208	8.44	8.38	8.309	9900	145	183
J0021+0052	CLASSY	0.09839	8.44	8.43	8.17[e]	9400	275	50
J032845.99+011150.8	VLT/XShooter	0.142181	8.30	8.41	8.30	9600	-	126
J015028.39+130858.4	VLT/XShooter	0.146712	8.17	8.33	8.30	10400	-	283
J124509.05+104340.1	VLT/XShooter	0.165569	8.48	8.41	8.54	9600	-	245
J005527.45−002148.7	VLT/XShooter	0.167449	8.37	8.39	8.47	9800	-	343
J101629.88+073404.9	VLT/XShooter	0.18271	8.18	8.16	8.33	12000	-	239
J082247.66+224144.0	VLT/XShooter	0.216226	8.19	8.15	8.39	12100	-	412
J084034.10+134451.3	VLT/XShooter	0.226961	8.30	8.27	8.37	10900	-	170
SGAS1723+34	JWST/NIRSpec	1.3293	8.17	8.12	8.13	12300	-	80
GOODS-N-14595	Keck/MOSFIRE	1.67596	7.86	7.89	>7.62	14500	391	-
GOODS-N-8240	Keck/MOSFIRE	1.6909	8.04	8.15	8.02	12100	377	-
RCSGA032727-132609	Keck/NIRSPEC	1.7	8.14/8.13[a]	8.15	8.19	12100	726	68
NIRSpec3753	JWST/NIRSpec	1.768	7.63	7.49	-	18200	-	275
CEERS-3506	JWST/NIRSpec	2.055	8.21	7.23	7.52	20700	-	3755
CEERS-3788	JWST/NIRSpec	2.295	8.16	8.11	7.91	12400	320	-
Sunburst Arc	JWST/NIRSpec	2.37	7.89	7.82	7.97	15100	1196	870
A1689-217	Keck/MOSFIRE	2.5918	7.87	7.69	8.06	16400	284	-
SGAS1226+21	JWST/NIRSpec	2.925	>7.94	>8.17	>8.04	<11900	-	489
Q2343-D40	JWST/NIRSpec	2.963	8.05	8.02	8.07	13300	-	73
Q2343-D40	JWST/NIRSpec	2.963	8.63	8.41	8.01[f]	9600	-	80
COSMOS-1908	MOSDEF	3.08	7.99	7.94	8.00	14000	491	-
CEERS-11088	JWST/NIRSpec	3.302	8.27	8.22	8.33	11400	-	175
CEERS-11088	JWST/NIRSpec	3.302	8.05	8.04	7.87[f]	13100	668	-
JADES-19519	JWST/NIRSpec	3.604	7.70	7.46	7.48	18500	58	-
GLASS-160133	JWST/NIRSpec	4.015	8.01	7.92	7.95[g]	14200	204	-
GTO1199-150880	JWST/NIRSpec	4.247	8.02	7.90	8.00	14400	-	195
GRB050505	JWST/NIRSpec	4.28	7.84	7.72	7.80	16100	73	53
CEERS-1665	JWST/NIRSpec	4.482	8.29	8.22	8.27	11400	-	217
CEERS-1665	JWST/NIRSpec	4.488	8.32	8.24	8.13	11200	1405	-
CEERS-1746	JWST/NIRSpec	4.56	7.92	7.77	7.95	15600	-	766
GLASS-150029	JWST/NIRSpec	4.584	7.71	7.54	7.53	17800	294	-
GLASS-150029	JWST/NIRSpec	4.584	7.76	7.66	7.70[g]	16600	143	-
ID60001	JWST/NIRSpec	4.6928	7.75	7.62	7.75	17000	-	236
EXCELS-121806	JWST/NIRSpec	5.225	7.94	7.85	7.97	14900	-	205
EXCELS-70864	JWST/NIRSpec	5.255	8.23	8.10	8.21	12500	-	~961[c]
J1211-0118	JWST/NIRSpec	6.031	>8.08	>8.09	8.51	<12600	226	-
J0217-0208	JWST/NIRSpec	6.204	8.22	8.16	8.20	12000	1526	-
J0217-0208	JWST/NIRSpec	6.204	8.07	8.01	-	13400	-	743
PJ308-21	JWST/NIRSpec	6.2342	7.99/8.02/8.07[b]	7.95	-	13900	-	1206
SXDF-NB1006-2	JWST/NIRSpec	7.212	7.98	7.94	7.99	14000	701	-
GLASS-10021	JWST/NIRSpec	7.286	7.88	7.67	7.87[g]	16500	61	-
ERO6355	JWST/NIRSpec	7.6651	8.24	8.12	8.24[h]	12300	1074	-
ZD12	JWST/NIRSpec	7.8762	7.30	6.71	7.34	25500	1007	-
JADES-GS-z8-0-LA	JWST/NIRSpec	8.48523	7.54	7.37	7.481	19300	2329	-
CEERS-1019	JWST/NIRSpec	8.6791	7.77	7.62	7.78[i]	17000	893	-
JADES-GS-z8-1-LA	JWST/NIRSpec	8.71523	7.72	7.52	7.699	17900	885	-
JADES-GS-z9-0	JWST/NIRSpec	9.4327	7.32	7.21	7.41	20800	743	-
MACS0647-JD1	JWST/NIRSpec	10.167	7.98	7.95	7.79[j]	13900	1613	-

[a] Left value is calculated by using $N_e[OII]$, and the right is by using $N_e[SII]$. Other galaxies with using both OII and SII electron density give same electron temperature and oxygen abundance, so they are just listed as one electron temperature and oxygen abundance value.

[b] From 3 assumptions of OII3726+OII3729 flux 0.5/1.0/2.0 respectively

[c] Upper limit of both SII lines are used to get the line ratio, so it is a uncertain value.

[d] Méndez-Delgado Formula. The uncertainty of 12 + log(O/H) derived by this formula for all galaxies is about 0.2.

[e] (Berg et al. 2022)

[f] (Bhattacharya et al. 2025)

[g] (Nakajima et al. 2023)

[h] (Curti et al. 2022)

[i] (Sanders et al. 2023)

[j] (Hsiao et al. 2024)